Optimizing the Radar Network Architecture for LEO Space Domain Awareness

J.J. Schuss
SpaceEM LLC
C.M. Cox
Keystone Mission Solutions Corporation

ABSTRACT

Space Domain Awareness (SDA) for the LEO orbital regime can be achieved by a global network of ground based radars, but this network will require a significant number of sensors to rapidly detect events or maneuvers, and to accurately determine changes in known satellite state vectors. The number of radars in this network may make it unaffordable if each radar is required to both carry out track and search/discovery over a large angular Field of View (FoV). However, the key network cost drivers can be mitigated by leveraging two architectural features into the system strategy: (1) use of a Limited Field of View (LFoV) radar architecture, and (2) distributing the total required global power-aperture among the network radars while maintaining event discovery timeliness for the system; here power is the average transmit radiated power and aperture is the effective area of the receive antenna. The result of this strategy is a network of smaller, lower cost radars, each having fewer phase-control elements, that maintains global system timeliness in detecting space events, and also provides for frequent track updates of known space objects. Effectively, this strategy distributes the function of orbital determination and discovery of space events over a global network of small radars. This paper will elucidate this architecture strategy, and show how a network of reduced power aperture LFoV radars can meet LEO needs at reduced cost and complexity.

1. INTRODUCTION

The population increase of LEO satellites over the last decade and mass launches of dozens at a time have clarified the need for rapid discovery and precision tracking of large numbers of space objects and events. Meeting this need requires a worldwide network of accurate, high sensitivity tracking radars that can rapidly detect new space objects or maneuvers that occur anywhere within the global LEO regime. Discovery of new objects or space events typically requires each radar to establish a wide angle surveillance fence that detects space objects that penetrate it. The angular extent of this fence is often of the order of $\pm 60°$ from zenith in order to assure that the space object is detected as it passes the radar. Once an object is detected, it needs to be tracked for some distance in order to establish or update its state vector and to predict its orbital path. The sensitivity of a radar in this surveillance or discovery mode scales as $\langle P \rangle A_r$, where $\langle P \rangle$ is the average radiated transmit power and A_r is the receive aperture area; the required $\langle P \rangle A_r$ also scales with the angular extent of the surveillance fence. Thus, in order to support a wide angle surveillance fence, large $\langle P \rangle A_r$ is required at each radar, which drives radar costs. In contrast, track sensitivity, even for a $\pm 60°$ Field of View (FoV), scales as $\langle P \rangle A_r A_t$, where A_t is the area of the transmit aperture (and in many cases $A_r \cong A_t$). From this simple scaling it is clear that increasing the transmit aperture area will drive down the required $\langle P \rangle A_r$ for track operation. For both track and surveillance operation, increasing $A_r \cong A_t$ will drive down the average radar transmitted power $\langle P \rangle$, which then reduces radar build and operating costs, and complexity. In order to leverage this cost reduction scaling, we need the cost increase due to the growth of both A_r and A_t to be much lower than the savings obtained from a reduced $\langle P \rangle$.

A complicating factor in growing A_r and A_t is that a full scan phased array, often required for agile tracking of space objects, requires phase control elements spaced approximately $\lambda/2$ apart. The number of such radar elements is then $4A_r/\lambda^2$ for receive and is a similar number for transmit. Since phase control elements, and associated Digital Beam Forming (DBF) networks are cost drivers, lowering the radar transmit power by increasing A_r and A_t can be a difficult strategy.

Finally, in order for the network to meet the timeliness requirements for detecting space events and updating known space object state vectors, many radars are required. If each radar has a large surveillance fence and full scan track capability, the cost of the network may be prohibitive, resulting in few radars actually being fielded. What is needed is a strategy for both reducing the required $\langle P \rangle A_r$ of each radar while cost effectively increasing A_r, in order to facilitate the fielding many low cost radars.

This paper presents a strategy for achieving a cost effective global network of small radars by leveraging two architectural approaches:

1) Use of a Limited Field of View (LFoV) architecture for the radars, and
2) Distributing the required global $<P>A_r$ among the network radars while maintaining the global timeliness of the network for discovery of new space events.

The LFoV architecture reduces $<P>A_r$ by increasing the spacing of phase control elements in the transmit and receive apertures and thereby reducing their quantities to much less than $4A_r/\lambda^2$. This thereby reduces the cost per unit area of the phased array aperture, facilitating a low cost increase in A_r and A_t and a resulting reduction in $<P>$. This reduction in $<P>$ not just simplifies the radar aperture, but also reduces its power consumption and operational costs. It should be noted that the LFoV architecture results in a reduction in the FoV scan volume in at least one dimension. Nevertheless, the FoV and radar operation can be optimized to yield accurate state vectors.

The second strategy of distributing the global $<P>A_r$ among the network radars is made possible by recognizing that global radar network event discovery time is a function of the total global radar power-aperture, not the individual radar power-apertures. As a result, we can reduce the angular width of each radar's search fence and each radar's power-aperture, while maintaining constant global power-aperture, and thereby achieve the same global discovery timeliness. We can then build a network of small, lower power, cost effective radars that permits rapid updates of space object state vectors while at the same time meeting global discovery timeliness needs.

The consequence of these two strategies is an alternative architectural approach for achieving LEO surveillance, namely fielding a global network of many, small radars, instead of deploying a network of a few, large radars. Both networks have comparable capabilities to discover new space events, but the large network of small radars provides for better custody of known space objects. Effectively, this latter radar system distributes the functions of orbital determination and discovery of space events over an expandable global network of small radars, the small radars being easier to instantiate and maintain in remote locations.

This paper will explain this architectural strategy and show how these factors can be leveraged to cost effectively optimize the global radar network. Section 2 will present the topology of a LFoV radar aperture and show how it can cost effectively reduce radar costs. The resulting reduced scan volume FoVs Section 2 can nevertheless yield accurate space object state vectors for updates of orbital parameters. Section 3 will show how $<P>A_r$ scales with surveillance fence width, and then show how we can utilize many small radars to maintain global system timeliness by conserving total system power-aperture; this strategy reduces the size and cost of each radar. Section 4 will present a more detailed astrodynamics analysis of timeliness and track errors for a generic LFoV radar and discuss its implications. Finally, Section 5 will summarize the key take-aways and conclusions of this study.

2. LFoV ARCHITECTURE AND TRACK

2.1 LFoV Architecture

The common feature of instantiations of the LFoV architecture is that the spacing, or effective spacing, of phase control elements on the array or aperture surface is much greater than $\lambda/2$ in at least one of the orthogonal array dimensions. Fig. 2.1-1 illustrates a generic topology of a LFoV array. Here the spacing of radiating elements and their phase control electronics in either the x direction (d_x) or the y direction (d_y) or in both directions is much greater than $\lambda/2$. Note that the phase control element is defined broadly; it can be any one of the following:

- a passive electronic phase shifter,
- a transmit module that includes a phase shifter,
- a receive module that includes a phase shifter,
- a transmit/receive module that includes a phase shifter, or
- an analog to digital converter (ADC) or a digital to analog converter (DAC) that interfaces the analog array to a digital beamforming back end, or
- a combination of the above.

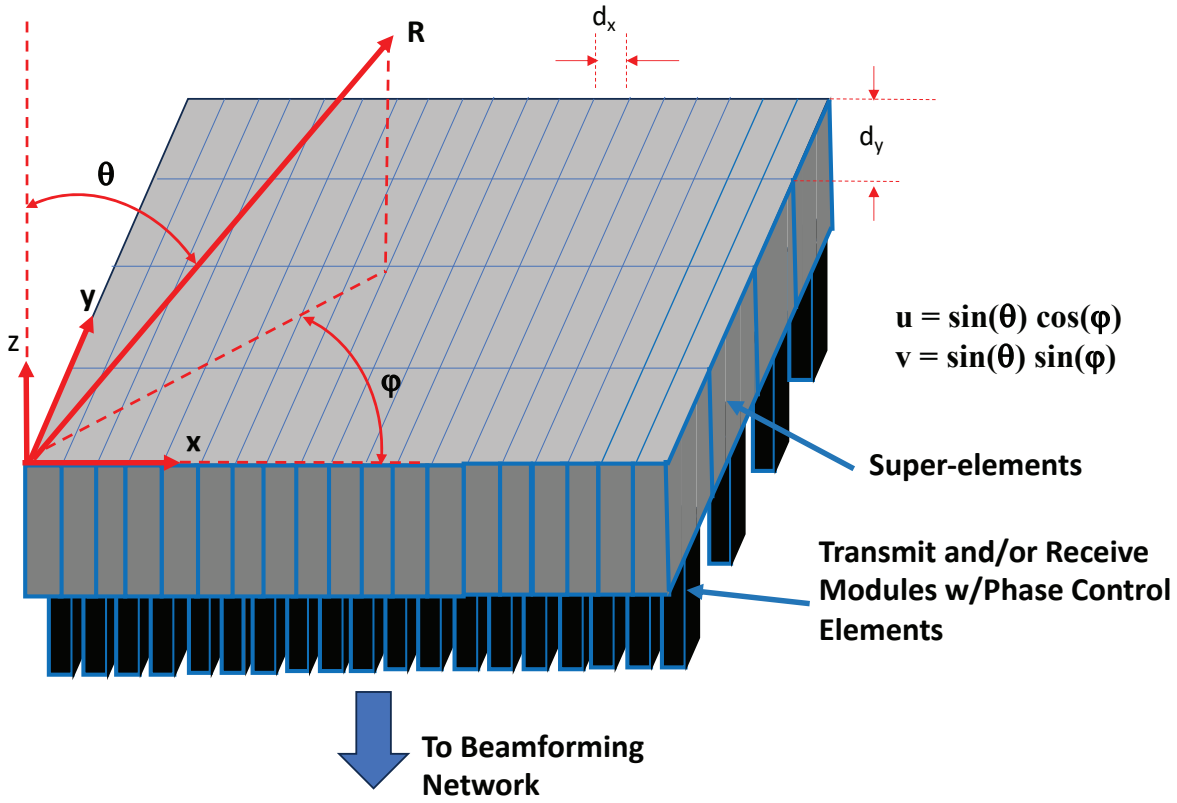

Fig. 2.1-1 – LFoV phased array generic topology. This shows a generic map of a LFoV phased array. Here $d_x \sim \lambda/2$ whereas $d_y >> \lambda/2$, and $d_x d_y >> \lambda^2/4$. Also shown are the definitions of the scan angle sines u, v which govern array beamforming and scanning. For $d_x \sim \lambda/2$ we obtain large scan angle operation in u, whereas in v scan performance is only obtained over a small scan angle range due to d_y being much greater than $\lambda/2$.

For these arrays to work efficiently, the radiating elements in the array aperture must effectively fill the space of the array with near uniform rf illumination, in order to preserve the array aperture efficiency. Aperture efficiency is defined as:

$$\eta = \frac{|\int dA\, E(x,y) \exp\,(jk(ux+vy)|^2}{A \int dA\, |E\,(x,y)^2\,|}$$

Here u, v are the angular sines in the direction of the radiated beam peak, A is the aperture area, and E is magnitude of the aperture E field illumination. For a perfect, uniform illuminated aperture with no phase errors, $\eta = 1$. Phased array elements that accomplish this, or approximately accomplish this, and have $d_x d_y >> \lambda^2/4$ are termed "super-elements," and are key to the LFoV architecture. Note that the 3 dB beamwidths of the super-element are equal to $\gamma\lambda/d_x$ in u and $\gamma\lambda/d_y$ in v, with γ being ~ 1; the exact value of γ depends on the details of the rf illumination in the aperture of the super-element. A perfect, uniformly illuminated super-element has $\gamma = 0.886$.

For the LFoV arrays discussed below, we desire the beamwidth in x to be very broad, so that the array can support a wide angular detection fence in x for detecting space objects; for a perfect radiating element that has $d_x = \lambda/2$, the super-element pattern in u will be $\cos(\sin^{-1}(u))$. This corresponds to a reduction of gain of 3 dB when $\sin^{-1}(u) = 60°$. For all cases discussed in this paper, we will assume $d_x = \lambda/2$ and $d_y >> \lambda/2$.

Fig. 2.1-2 shows some topology variants of the LFoV aperture. (a) shows an example of waveguide type super-elements, where one of the waveguide dimensions is much greater than $\lambda/2$. This leads to a narrow angular scan

volume in the v direction. (b) shows a corporate feed type of super-element. If all of the elements are in phase, the radiated field characteristics of this type of super-element are similar to those of the waveguide super-element. However, if the corporate feed imposes a phase gradient in the y direction, the scan volume in v will be shifted off of v=0. Similarly, if the corporate feed imposes a line length gradient in the y direction, the offset of the scan volume will move with frequency. Either effect can be utilized to optimize the super-element efficacy in tracking space objects.

Fig. 2.1-2c show a space fed reflector antenna topology. In this case, the effective area of each radiating element in the rf feed is effectively magnified to be larger by the reflector optics. While this type of LFoV aperture is physically different from that of (a) or (b), its performance can be similar.

Finally, figures 2.1-2d and 2.1-2e shows two variants of the LFoV aperture. In fig. 2.1-2d a single aperture provides for both the transmit and receive functions, whereas in fig. 2e one aperture is used exclusively for transmit and the other aperture for receive. Both approaches have advantages and disadvantages depending on the application, and both approaches can take advantage of the LFoV architecture.

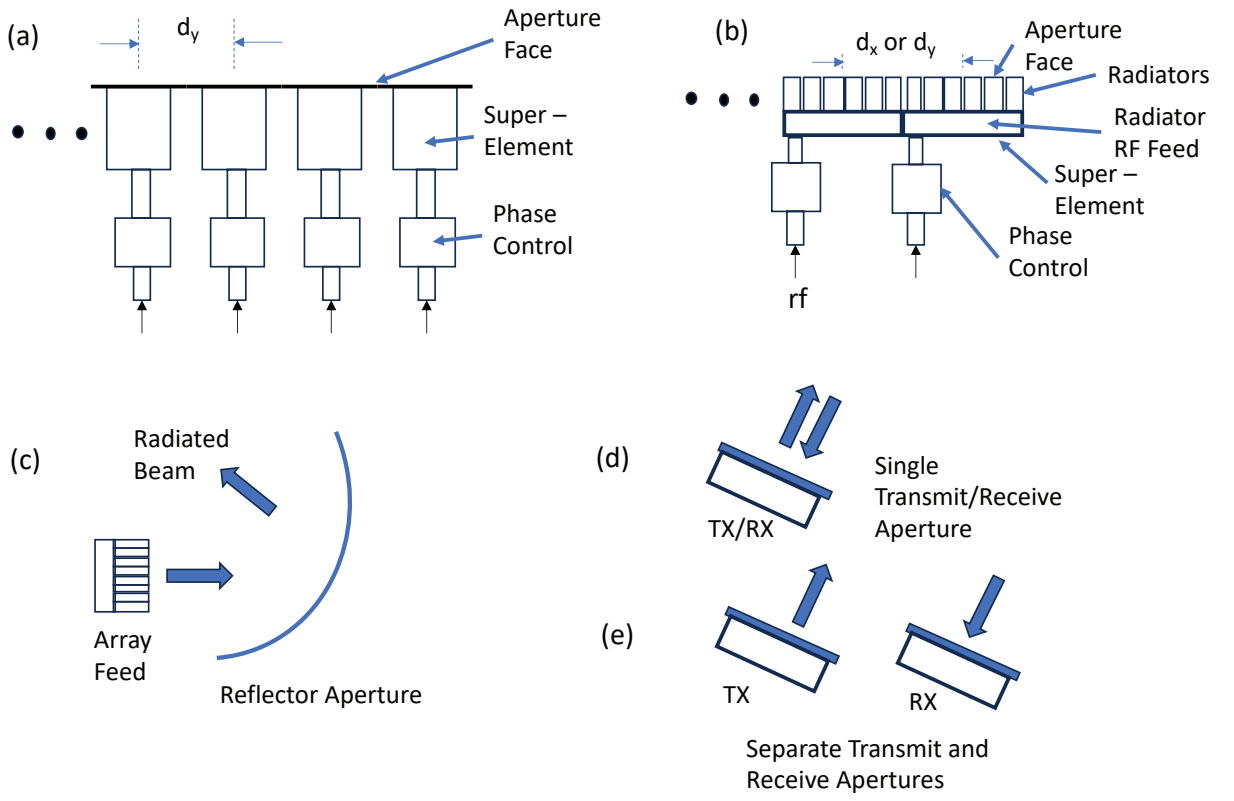

Fig. 2.1-2 – LFoV architectural examples, corresponding to Fig. 2.1-1. (a - c) shows generic LFoV antenna examples, including (a) waveguide super-elements, (b) corporate fed super-elements, and (c) space-fed reflector antennas. (d) illustrates a single transmit/receive (TX/RX) aperture antenna, whereas (e) illustrates separate TX and RX aperture antennas.

Fig. 2.1-3 shows a cross section view of the radar fence that is assumed in this paper. In all cases, the fence extends in u which is approximately in the x direction. The radar supports a surveillance fence of angular width 2θ at altitude h. This fence is designed to detect and track any object of radar cross section σ that crosses it, whether or not this object is known or unknown. Since the fence must detect an object that can appear anywhere in the 2θ width fence, a significant amount of radar resources must be expended to support it. A track fence is also shown, which is usually wider than the surveillance fence. The track fence is designed to track a known object that will

impinge on the fence at a known altitude, angle, and time. Since these details are known, the radar only needs to place a focused beam at the location where the space object will cross, and therefore much reduced radar resources are needed to support this track fence relative to the surveillance fence.

Fig. 2.1-4 shows a mapping in u-v space of a possible FoV of a LFoV radar. In this map, u=v=0 corresponds to a zenith (boresight) rf beam from the radar, and the circle at $u^2 + v^2 = 1$ corresponds to an endfire rf beam from the radar aimed at the horizon. The FoV boundaries are shown in blue; here we assume an FoV that extends in u from -0.85 to +0.85, and in v has a width of 0.1. The FoV is centered at v = 0.2. The red lines show examples of orbits that penetrate the FoV at different values of u, where we have selected orbits that are perpendicular to the u axis when they cross it. Here we refer to this FoV with a width dv = 0.1 as a "thin" FoV. We will also consider a "thick" FoV having dv = 0.3, centered at the same v = 0.2.

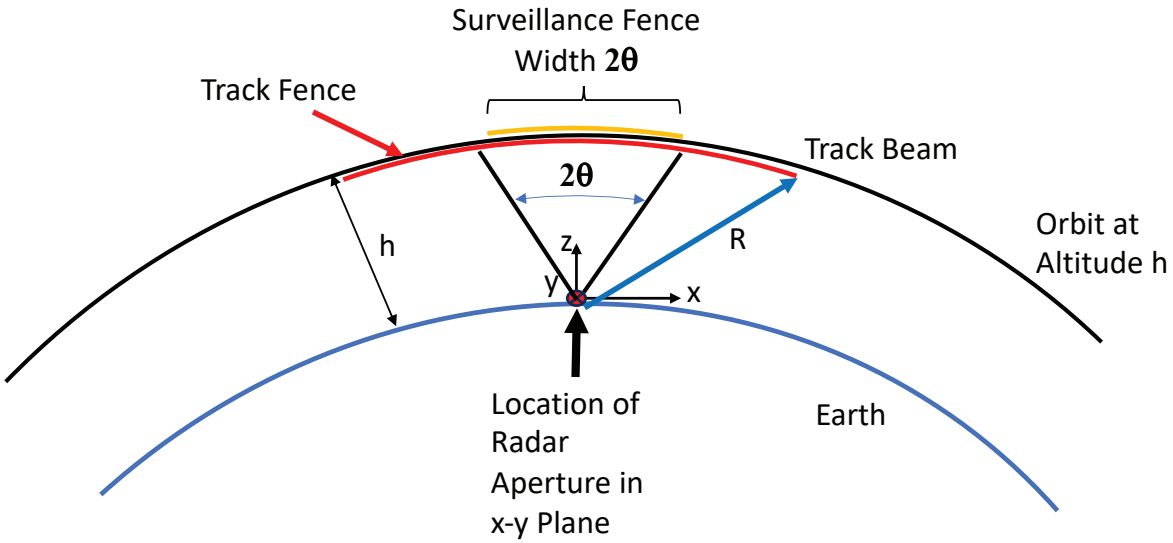

Fig. 2.1-3 – Geometry for analysis of radar sensor. Radar sensor is located at x, y, z = 0, with the radar aperture pointed to zenith. The fence is analyzed at altitude h above earth. Surveillance fence total width is 2θ; also shown is track beam focused on object distance R from radar. The track fence is the region in space where if a known space object crosses it, the radar can track it through the FoV. In general, the track fence is much wider than the surveillance fence.

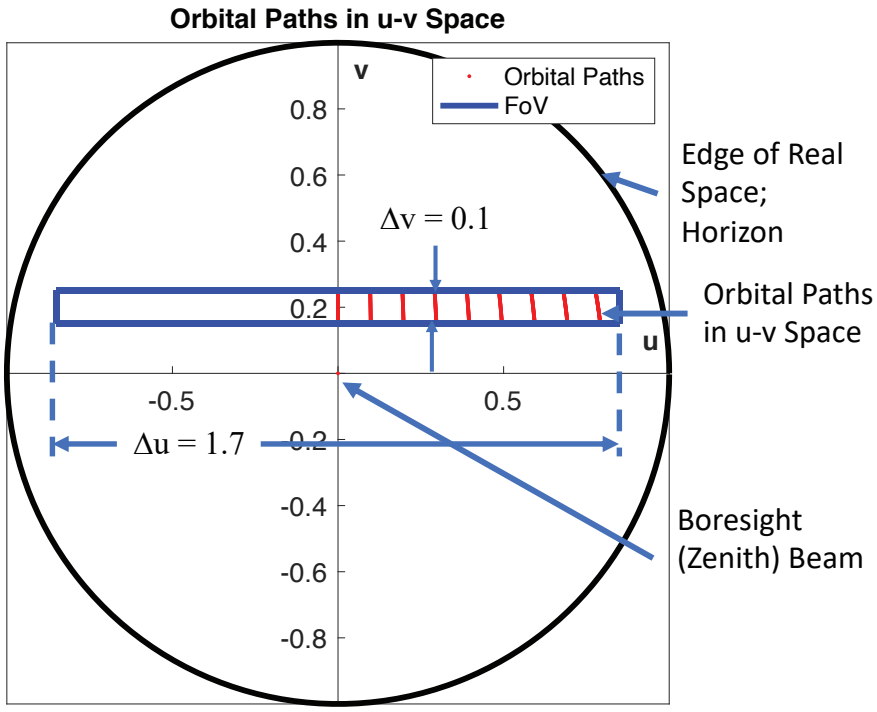

Fig. 2.1-4 – Angular coverage map of typical LFoV radar aperture. Here the radar covers a narrow swath in v that is also offset from boresight; coverage in u is much broader and extends to ± 61°. Red lines indicate orbital paths that will be analyzed, mapped into u-v space.

In Section 4 the orbit estimation accuracy of the orbits that cross these FoVs will be considered. In doing this analysis we will assume the following 1-σ errors for each track pulse measurement:

- Doppler velocity error: $\sigma_{DOP} = 1.04\ c\ /(\tau_{DOP}\ 2f\ BS)$, where τ_{DOP} is the time duration of the Doppler waveform, c is the speed of light, f is the operating frequency (here assumed to be S-Band), and BS is the beamsplitting factor (here conservatively assumed to be 20). We will also assume in this example that τ_{DOP} = 50 msec.

- Range error: $\sigma_{RANGE} = \Delta x_{RANGE}/BS$, where Δx_{RANGE} is the 3 dB width of a range cell, and is assumed to be 20m.

- u error: $\sigma_u = BW_u/BS$, where BW_u is the array beamwidth in sine space in the u direction, and is assumed to be 0.012.

- v error: $\sigma_v = BW_v/BS$, where BW_v is the array beamwidth in sine space in the v direction, and is assumed to be 0.003. Note that we have assumed that $BW_v << BW_u$.

3. GLOBAL SHARING OF POWER – APERTURE FOR SEARCH

3.1 Power – Aperture and Radar Scaling

As illustrated in fig. 2.1-3, the track fence of a space surveillance radar is generally wider than the surveillance fence. The reason for this is that the track fence of the radar only needs to place a narrow focused beam on the known target; the focused beam angular width is typically of the order of 1°. For radar surveillance, however, the fence may be much wider (~ ±60°) since we are trying to detect and discover unknown objects whose penetration

location of the FoV is unknown. Since the radar must spread its transmit power over a large angle in u-v space, which is much larger than the ~ 1° track beam width, a radar that supports a wide surveillance fence will be larger and more expensive than one that only provides for tracking known objects.

In order to meet LEO SDA needs for timeliness, which is the time required to update space object state vectors or the time required to discover new space events, many radars are needed in a global network. Often, large surveillance fences are prescribed for each radar for discovery of unknown objects or events, in addition to wide track fences. As will be shown here, wide surveillance fences dictate radars having large $<P>A_r$, where <P> is the average transmit power of the radar, and A_r is the effective receive aperture area. Large $<P>A_r$ increases the size and cost of a radar, and can make a global LEO multi-radar network unaffordable.

There is an architecture solution to this dilemma, if we note that discovery timeliness is a function of the total global $<P>A_r$; that is, timeliness is a function of the sum of the $<P>A_r$'s of the network radars. This implies that timeliness needs can be achieved using more but smaller radars, each radar having a wide track fence, but only a narrow surveillance fence. The result is a larger network of radars and more rapid updates of known space object state vectors. This makes a large LEO radar network that meets both track update and discovery timeliness affordable. The basis for this architectural approach is presented below using a simple, top level radar scaling analysis.

Radar scaling starts with the radar equation

$$\text{SNR} = \frac{<P>\tau\,\sigma_{RCS} A_r G_t L}{(4\pi R^2)^2\, kT_a} \quad > \text{SNR}_o \tag{1}$$

where SNR_o is the required signal to noise ratio, R is the distance to the target, T_a is the antenna noise temperature, σ_{RCS} is the space object RCS, G_t is the transmit gain on the target, τ is the total time the target is illuminated with average transmit power <P>, and L is the product of losses in the system (transmit ohmic, similarity, signal processing, etc.). Here we assume that the entire radar's resources are dedicated to surveillance; usually, the radar will be designed somewhat larger than this to provide for other functions, but there are other sizing strategies that can be followed.

We further assume that we are detecting space objects that are in orbits that perpendicularly cross the surveillance fence, and that we coherently integrate transmit pulses for a time τ equal to the transmit time of a space object across the 3 dB beamwidth of the radar in v (the narrow beamwidth direction). This sets

$$\tau = \gamma_{tr} \frac{\lambda R}{D_y v_t} \left(1 + \frac{v_o}{R} \frac{\partial R}{\partial v}\right) \tag{2}$$

Here R = R(u, v) is the distance to the target, D_y is the (longer) direction of the radar aperture in the y direction, v_o is the location of the surveillance fence in v (typically v_o is 0 or << 1), v_t is the velocity of the space object, and

$$\gamma_{tr} = \frac{\gamma_{rx}\gamma_{tx}}{\sqrt{\gamma_{rx}^2 + \gamma_{tx}^2}} \tag{3}$$

where $\gamma_{rx} = 1.05$ and is the receive beamwidth factor, and γ_{tx} = 0.886 and is the transmit beamwidth factor. γ_{tr} is the combined transmit/receive beamfactor in v and gives the effective 3 dB beamwidth of the radar in that dimension.

We can now prescribe a surveillance radar that perfectly distributes its transmit power over the surveillance fence so as to achieve the same SNR everywhere. This leads to a required $<P>A_r$:

$$<P>A_r = \text{SNR}_o \frac{4\pi v_t kT_a\, Q(\Delta u, v_o)}{L\sigma_{RCS}\gamma_{tr}} \tag{4}$$

where

$$Q(\Delta u, v_o) = \int_{-\Delta u/2}^{\Delta u/2} du \; \frac{R^3}{cos^2\theta \sqrt{1-v_o^2 R^2/(a+h)^2}} \tag{4a}$$

Here $-\Delta u/2 < u < \Delta u/2$ defines the width of the fence in u.

In comparison, we can obtain the minimum $<P_o>A_r$ required to support track at angle θ_o and distance to target R_o as

$$<P_o>A_r = SNR_o \frac{4\pi v_t k T_a R_o^3 \frac{\lambda}{D_x}}{L\sigma_{RCS}\gamma_{tr} cos^2\theta_o \sqrt{1-v_o^2 R_o^2/(a+h)^2}} \tag{5}$$

again assuming that all radar resources are dedicated to track. We can now obtain β as the ratio of the power – aperture to surveil a fence of width Δu to the power – aperture needed to track a space object at θ_o, R_o:

$$\frac{<P>A_r}{<P_o>A_r} \equiv \beta = \frac{Q(\Delta u, v_o)\, cos^2\theta \sqrt{1-v_o^2 R_0^2/(a+h)^2}}{\lambda/D_x \, R_o^3} \tag{6}$$

Equation (6) approximately shows that for small angles, β scales linearly with Δu. This relationship is shown in Fig. 3.1-1, where we graph β vs. the half width of the surveillance fence in degrees; here β is normalized to $<P_o>A_r$ at 60° and 1500 km. Starting at ~ 20° to 30° β starts to significantly increase over a linear relationship, mainly due to the increase in R^3 and decrease in cosθ at large angles. For the case shown, a radar sized for track at 1500 km and 60° scan can support a surveillance fence at 1500 km altitude of ± 6° at boresight, and can support much larger angles for surveillance at lower altitudes. This indicates that this tracking radar on average has margin in its capabilities to track known space objects whose orbits are uncertain.

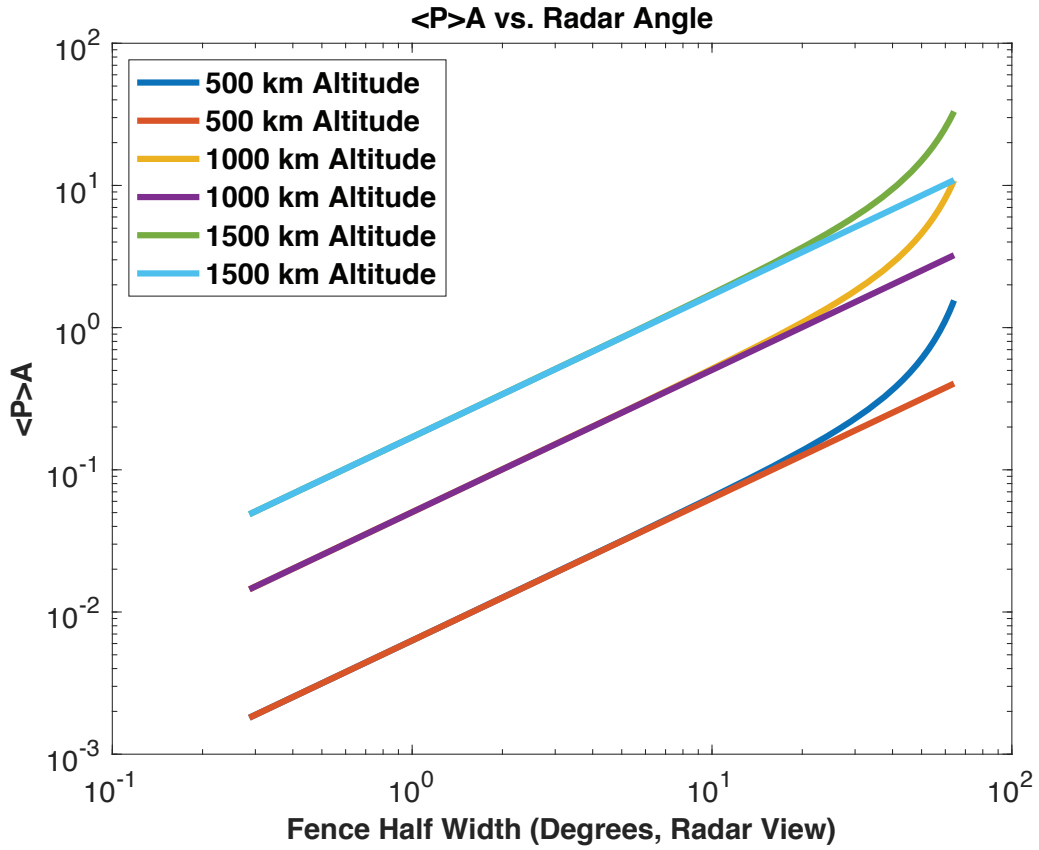

Fig. 3.1-1 – Required <P>A vs. surveillance fence width for orbits at altitudes of 500 km, 1000 km, and 1500 km. For larger angles required <P>A is no longer proportional to fence width, and is larger than this linear relationship. <P>A is normalized to the required $<P_o>A$ to track a single space object at 60° scan off boresight and at 1500 km altitude; calculation is done for $\lambda/D_x = 0.02$. Here $v_o = 0.1$.

3.2 Timeliness for Detection of LEO Space Events for Constant $<P>A_r$

Equation 6 and Fig. 3.1-1 show how $<P>A_r$ scales with fence width for a LEO surveillance radar. Here we calculate how timeliness for detection of space events varies with the number of global radars in a network, for global $<P>A_r$ kept constant, and for a simplified scenario. We analyze perfect circular orbits at altitudes of 500 km, 1000 km, and 1500 km, with the orbits distributed over inclinations of 45° to 90°. The orbits are also distributed from 0° to 360° in the longitude of their ascending node, and also from 0° to 360° in their starting angle in their orbital plane. The radar network configurations analyzed have either 1, 5, 10, or 20 global radars. For the single radar case, the radar is sited at 3° latitude, and has a surveillance fence of ±60° for altitudes of 1000 km and 1500 km; for 500 km, the radar has a surveillance fence of ±66°. As the number of radars is increased, the $<P>A_r$ of each radar is decreased so that the total sum of the radars' $<P>A_r$ is unchanged from the single radar case. For the 5 radar case, the radars are situated at a 3° latitude and distributed approximately uniformly in longitude. For the 10 radar and 20 radar cases, 30% of the radars are located at 45° latitude, 30% of the radars are located at -45° latitude, and 40% of the radars are located at 3° latitude. All radars at each latitude are approximately uniformly distributed in longitude.

Fig. 3.2-1 shows typical propagated orbits for the single radar and the 10 radar cases. Orbits are propagated until they cross a radar fence, which is when the time since the orbit started is tabulated. Using these statistics, the mean time to detect and the 90% confidence time to detect are calculated. These results are shown in fig. 3.2-2.

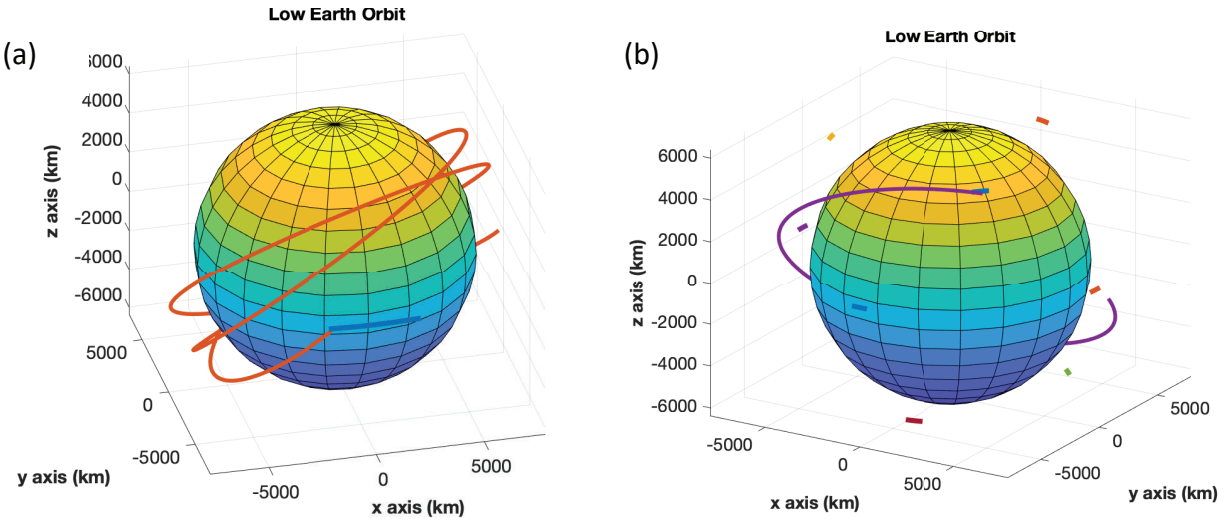

Fig. 3.2-1 – Typical circular orbits analyzed vs. number of sensors and fence sizes. Here the altitude of orbits is 1500 km; for (a) there is 1 sensor whereas for (b) there are 10 sensors having the same total global power-aperture as the single sensor in (a). Note that fences are slightly curved in earth coordinates, since the fences are at constant v, not constant latitude. Orbit is tabulated when it passes through a radar fence.

Fig. 3.2-2 plots the mean time and 90% confidence time to detect an unknown object vs. the number of radars, for 500 km, 1000 km, and 1500 km altitudes. In all cases, the total global <P>Ar is approximately unchanged. Fig. 3.2-2 shows that these timeliness metrics are roughly constant as the number of radars grows. In fact, for lower altitude space objects, timeliness improves as the number of radars increases.

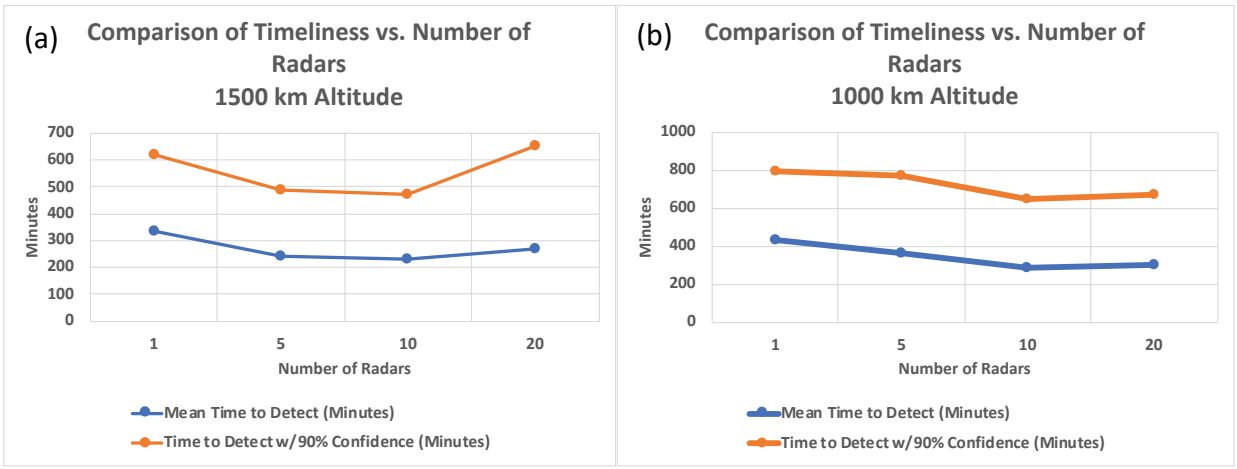

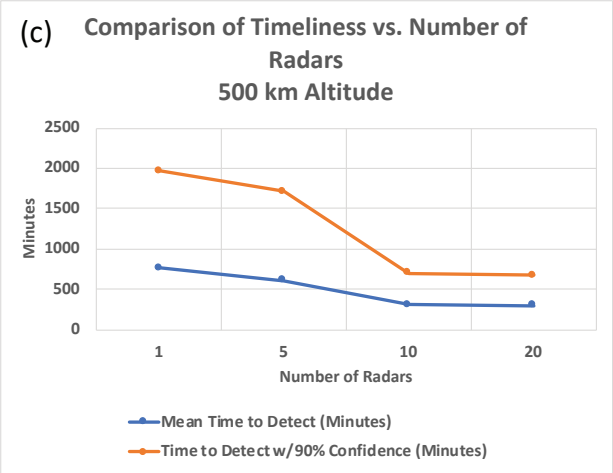

Fig. 3.2-2 – Mean time to detect and 90% confidence time to detect for object in circular orbit vs. number of radars, keeping global power-aperture constant. (a) – (c) tabulate results for altitudes of 1500 km, 1000 km, and 500 km. Note that as altitude decreases, the detection times improve as the number of radars grows.

We have also calculated the mean time and the 90% confidence time to track a known object for these radar networks; these statistics can be compiled by running the simulation with ±60° fences. For 10 global radars and a space object at 1000 km altitude, the mean time to track is 39 minutes, and 90% confidence time is 106 minutes. This means that a 10 radar global network will update track information on known space objects in roughly 1 hour, while at the same time discovering new space events on a time scale of 5 – 10 hours. The implication is that a global network of 10 small radars will facilitate measurements of space objects on an hourly scale, permitting rapid and accurate determination of the object's state vector, all while enabling discovery timeliness on a time scale of 5-10 hours.

Finally, it should be noted that the radar of Fig. 3.2-2 that is sized for tracking at 60° scan angle and at 1500 km will support a surveillance fence at boresight of ±19° at 1000 km and ±58° at 500 km. Thus, even for small radars sized for track at higher altitudes, significant surveillance and discovery capabilities are enabled and enhanced at lower altitudes.

3.3 Cost Scaling of LFoV Radars

The previous analysis has shown that a network of small radars, each having a LFoV architecture as well as reduced $\langle P \rangle A_r$, can enable accurate space object tracking as well as the rapid discovery of space events. The ultimate viability of such a network is determined by both performance *and* cost. Radar cost decreases as $\langle P \rangle A_r$ is reduced, and further decreases depending on the how effectively the LFoV architecture is leveraged. While detailed costs change rapidly as technology advances, a rough cost framework can be outlined.

The cost of a LEO space radar can be estimated based on the top level scaling

$$Cost = C_o + \frac{A_r\, C_1\, F_{LFoV}}{(\lambda/2)^2 F_{AREA}} + \frac{A_t}{(\lambda/2)^2 F_{AREA}} \left[F_{LFoV} C_2 + C_3 P_o\right] \qquad (7)$$

Here C_o is the fixed site and equipment cost, C_1 is the cost per receive element, C_2 is the cost per transmit element, F_{AREA} is the factor of how large each elements aperture area is compared to $(\lambda/2)^2$, F_{LFoV} is the factor of how much more the aperture area of a super-element costs for the LFoV array compared to the cost of an element's area for a full scan array, C_3 is the additional cost per transmit element per watt radiated power, and P_o is the average rf power per transmit element. Note $(A_t/[(\lambda/2)^2 F_{AREA}]$ is the number of transmit elements N_t, $N_t P_o = \langle P \rangle$, and for the combined transmit/receive aperture topology of fig. 2d, $F_{LFoV} C_2 << C_3 P_o$. From this generic scaling we observe the following:

- The LFoV approach will be successful in cost effectively growing A_r, and thereby reducing <P> and the transmit cost (3rd factor in equation (17)), to the extent that $F_{LFoV}/F_{AREA} \ll 1$. For $F_{LFoV}/F_{AREA} \sim 1$ the LFoV approach will likely fail. This puts a priority in utilizing a super-element whose cost per aperture element is roughly the same as the cost per aperture element of a conventional radiator.
- As <P> is reduced, we can either reduce N_t or reduce P_o. This reduces the transmit cost of the radar, and depending on the radar design may be the dominant cost of the radar.

It should also be noted that the power consumption of the radar is usually dominated by the transmitter power draw. As a result, as <P> is reduced, the power consumption of the radar is strongly reduced, which is often the largest operating cost of the radar.

4. ASTRODYNAMIC ANALYSIS

4.1 Astrodynamics Analysis Tool and Technique

Astrodynamics analysis of the visibility and track accuracy was performed using the ORAN Orbit Analysis tool originally developed by NASA [1-4]. This tool performs a full covariance analysis and propagation of orbit uncertainties resulting from user specified racking configurations for multiple data types. The code can compute and propagate the noise only covariance terms, including the effects of the equations of motions for the orbital applications, as well as modeling effects of observational and force model errors. The code is used here to assess geometric visibilities as well as track accuracy, and maneuver estimation uncertainties. Key results are:

- More sensors result in better timeliness, and faster detection of orbital maneuvers for known space objects.
- More sensors result in reduced SPOE (Single Pass Orbit Estimates) in fence penetration at the next sensor, due to better timeliness.
- Thick FoVs give higher accuracy SPOEs than thin FoVs, but thinner FoVs are acceptable for a network of ~ 10 sensors.
- Networks of ~10 sensors give more accurate multi-day orbit solutions than a single global sensor.
- Networks of ~10 sensors have a higher probability of not losing custody of maneuvering objects.
- Maneuver accelerations can be estimated using pre- and post- maneuver tracks.

4.2 Visibility and Timeliness

Timeliness of track updates has been quantified in terms of the average time between detections as a function of the number of sites within the network of radars. Up to ten sensors were considered, spread in longitude around the world, and evenly divided between northern and southern hemisphere at 33 degrees latitude, north and south. All sensor FoVs are oriented East/West. As the example sensor FoV is offset slightly from vertical, the FoV was shifted towards the equator to slightly increase the number of RSOs that can be tracked below the site latitudes.

Sensor FOV width is shown in Table 4.2-1 below for the cued (tracking known space objects) and uncued (discovery of unknown space objects) operating modes. All run cases used a v (or North/South) tracking extent of ~17.5° (0.3 sines). In Table 4.2-1 the uncued fence size is determined by the assumed requirement for a +/- 10° discovery fence at 1500 km altitude for a network of 10 radars; for fewer radars, a larger uncued discovery fence would likely be used to achieve better timeliness. At lower altitudes the +/-10° fence at 1500 km translates to a wider uncued search extent for a similar sized RSO.

Table 4.2-1 Cued and Uncued search mode sensor FOV width

Altitude (km)	Uncued FOV Width	Cued FOV Width
1500	+/- 10°	+/- 60°
1000	+/- 29°	+/- 60°
700	+/- 51°	+/- 60°
500	+/- 65°	+/- 65°

For these examples, a 3-day period is assumed for the averaging. The initial track starts top dead center at the first sensor field of view entry point. While longer modeling periods will yield a more consistent "average" time as the sample period increases, this example period is also a useful orbit determination solution arc length for a multiday orbit solution.

Cued detection timeliness is shown in Figure 4.2-1. For the given FoV width, the average time between detections will decrease as altitude increases for 1-10 sensors as the relative fraction of the projected longitude in view of the FOV increases with altitude. Put another way, there is less opportunity for object to under fly the edge of the FOV. For the uncued performance shown in Figure 4.2-2 the timeliness degrades with altitude due to the smaller extent of the coverage for the uncued search as altitude increases. In this case more radar power-aperture will permit a wider uncued fence and improve the timeliness, up to the limit defined by the sensor FoV and orbit mechanics, as illustrated in Figure 4.2-1

These results are independent of the RSO RCS or sensor power – the radar detection performance has been defined at a given altitude, not range. In this case the improvement in timeliness for any given altitude is driven by the number of sensors.

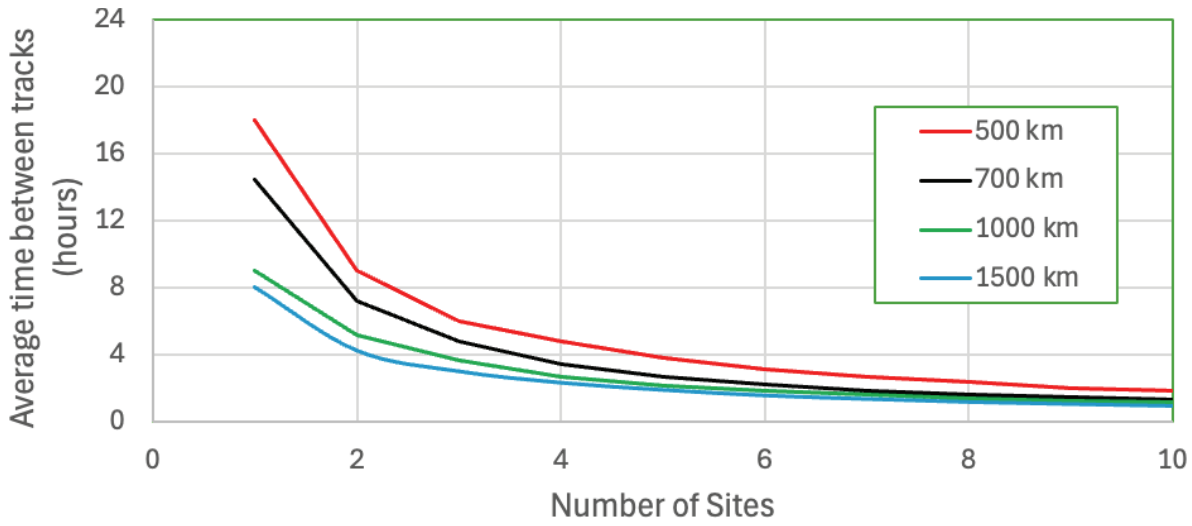

Figure 4.2-1. Cued timeliness vs number of sites, shown as average time between RSO tracks vs number of sites.

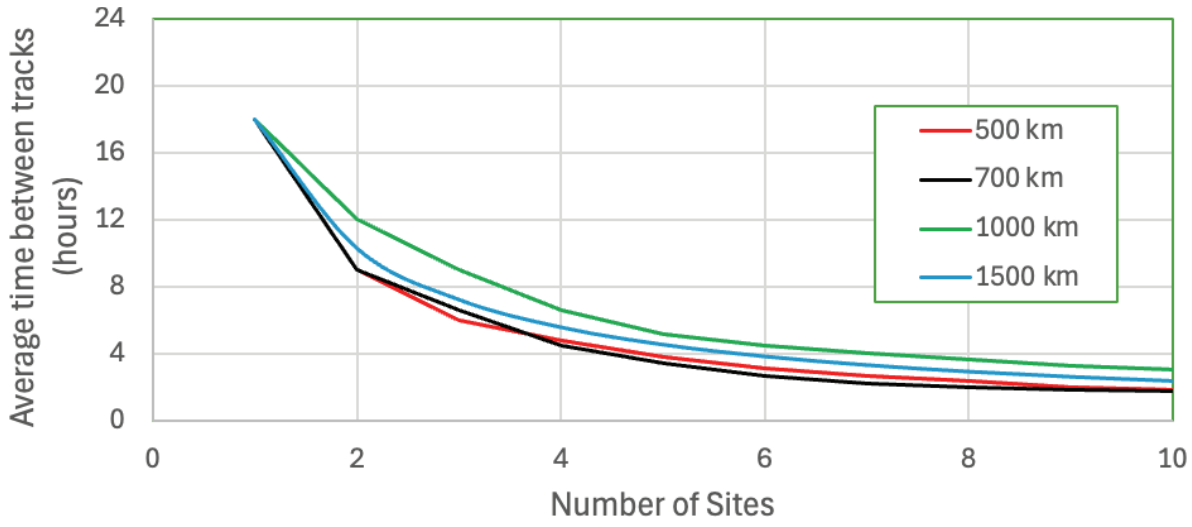

Figure 4.2-2. Uncued timeliness vs number of sites, shown as average time between RSO tracks vs number of sites. Uncued fence sizes from Table 4.2-1 are used here.

The authors have performed extensive analysis in the past for siting of multiple Space Fence class sensors. Real world constraints – for example available dry land – will limit possible bed locations for the sensors. Likewise, the latitude and orientation of the sensors may be constrained. Detailed selection of possible sites can somewhat optimize the performance of the network in terms of catalog completeness and timeliness for specific classes of RSO at different orbit inclinations.

4.3 Orbit Determination and Prediction Accuracy

4.3.1 Initial Orbit Determination Accuracy

Single track orbit solution estimates were computed for a range of altitudes, location of entry into the FOV, and azimuth of entry, with respect to true north, for two FOV options. The first case is a narrow FOV where the FOV fan is only 5.7° (0.1 sines) "thick", with a nominal fan width of +/- 60° from boresite. For ease of discussion this case in the "thin" FOV case. The second case used a thicker FOV of 17.5° (0.3 sines), the "thick" FOV case. Both cases consider a circular orbit encountering an East-West oriented FOV Fan. The fans were offset slightly towards the equator, and the RSO is on an ascending leg of the orbit passing from south to north through the FoV. An azimuth of 0° (with respect to north) is a 90° inclination. The 30° and 60° azimuths cases were set to fly towards the center of the FOV to avoid flying out the side of the FOV.

Table 4.3-1 shows the Single Pass Orbit Errors noise only track errors for the "thin" and the "thick" FoV cases. A key component of these tracking errors is the in-track velocity, which provides a basic measure of the prediction accuracy for the track solution. This velocity error is a principal measure of the orbit period uncertainty, which is the key term driving orbit prediction error growth over time. In all cases penetration perpendicular to the FOV, resulting in the shortest tracks, yielded the highest velocity errors. At angles in the fence off the boresite, the time of flight (ToF) through the FOV increases, also reducing errors. As the penetration azimuth increases, the errors similarly reduce.

Comparison of the thick vs. thin cases yields some interesting insights. The 3x longer ToF will produce 3x more observations at a constant track rate which is expected to reduce the noise-only formal errors by $\sqrt{3}$. This is seen in the position uncertainties, which are to first order driven by the angular uncertainties. The velocity error reduction is closer to $3^{1.5}$X. In addition to the longer time of flight in the FoV bringing in more observations, the longer ToF brings in more range and range rate data which helps to decorrelate the covariance matrix and improve the estimate of velocity.

In general, the shortest flight time geometry through the FOV is ***not*** representative of the overall performance of the system. The actual performance of any given sensor will depend on the site location, the orientation of the fence, whether east-west or turned, and the actual distribution of RSO orbits in the catalog.

Figure 4.3-1 shows the average SPOE noise only prediction accuracy at the next sensor fence contact based on the average time between contacts, for both the thin and thick fence options. For this graphic the prediction accuracy for each of the 9 entry geometries was averaged. This approach represents the expected typical performance by weighting the higher errors encountered for the 0° azimuth fly throughs. With the bulk of the RSO catalog at higher inclinations it is expected that an East-West fence will have most fly throughs in an azimuth range of 0°-30°.

This analysis is primarily concerned with the noise only errors and their growth, as this provides a measure of the relative sensor performance between different configurations. Drag is potentially a large contributor in prediction error; however, in the case of the SPOE predication error performance it is much smaller than the noise-only error contribution for a nominal active spacecraft with a low area to mass ratio. For very small debris with a high area to mass ratio, the contribution of drag can be larger. However, the intended use for this class of sensor system is for maintaining custody on active spacecraft.

Table 4.3 -1. Single pass noise-only orbit estimate accuracy (1σ)

FOV Thickness	Alt (km)	Penetration Azimuth Angle	Angle in Fence	Position (m)			Velocity (m/s)		
				Radial	Cross-track	Along-track	Radial	Cross-track	Along-track
5.7°	500	0	0	3.9	134.7	16.0	0.36	27.86	1.43
			30	71.0	141.9	16.7	12.06	24.35	1.08
(0.1 sines)			60	197.0	152.0	22.2	21.95	17.28	0.42
		30	0	6.2	67.0	29.5	1.34	11.60	0.53
			30	31.8	69.3	31.2	2.22	7.92	0.32
			60	107.6	77.9	46.4	4.33	5.12	0.15
		60	0	5.0	30.8	35.7	0.77	3.00	0.09
			30	19.9	31.8	33.9	0.49	1.98	0.07
			60	56.4	29.3	38.9	0.54	0.95	0.06
	700	0	0	4.3	144.3	18.4	0.31	22.74	1.19
			30	68.0	139.9	19.3	9.72	20.31	0.90
			60	239.9	199.1	30.4	21.86	18.59	0.41
		30	0	7.7	82.8	34.3	1.07	9.40	0.43
			30	35.4	73.9	37.6	1.81	6.58	0.26
			60	127.3	94.1	62.0	3.87	4.96	0.15
		60	0	6.3	38.3	42.0	0.63	2.50	0.08
			30	22.6	32.5	40.0	0.40	1.58	0.05
			60	65.9	32.5	49.4	0.45	0.86	0.07
	1000	0	0	4.7	157.7	21.6	0.24	18.52	0.99
			30	74.6	162.5	23.1	7.38	16.39	0.71
			60	250.3	228.7	41.4	18.44	17.50	0.39
		30	0	7.8	91.4	40.4	0.81	7.63	0.36
			30	39.2	84.3	45.3	1.33	5.17	0.21
			60	149.6	117.0	84.7	3.39	4.88	0.16
		60	0	6.4	42.9	49.4	0.48	2.02	0.06
			30	25.1	36.7	47.1	0.31	1.23	0.05
			60	76.7	38.7	64.4	0.38	0.81	0.08
17.5°	500	0	0	3.0	66.1	8.9	0.14	5.17	0.27
			30	34.2	68.3	9.4	2.18	4.44	0.16
(0.3 sines)			60	82.8	63.2	12.9	2.44	1.95	0.06
		30	0	5.1	38.1	16.8	0.41	2.14	0.09
			30	17.4	36.7	17.9	0.43	1.58	0.06
			60	54.7	38.9	25.1	0.73	0.93	0.05
		60	0	4.2	18.2	21.0	0.32	0.59	0.02
			30	11.2	16.8	18.7	0.28	0.43	0.03
			60	19.1	14.9	13.3	0.18	0.22	0.03
	700	0	0	3.6	82.2	10.7	0.12	4.37	0.23
			30	36.4	75.0	11.1	1.67	3.53	0.12
			60	86.2	70.9	16.1	1.63	1.43	0.07
		30	0	6.3	46.7	19.8	0.33	1.79	0.07
			30	19.6	41.4	21.3	0.34	1.27	0.05
			60	86.2	70.9	16.1	1.63	1.43	0.07
		60	0	5.2	22.3	24.5	0.26	0.50	0.02
			30	12.1	18.5	20.9	0.21	0.34	0.02
			60	86.2	70.9	16.1	1.63	1.43	0.07
	1000	0	0	4.0	91.4	12.5	0.09	3.53	0.19
			30	38.8	84.1	13.2	1.21	2.72	0.08
			60	89.6	80.7	20.9	1.07	1.05	0.07
		30	0	6.5	52.9	23.3	0.25	1.46	0.06
			30	21.9	47.4	25.7	0.26	1.01	0.04
			60	60.6	46.6	37.5	0.35	0.55	0.06
		60	0	5.4	25.3	28.2	0.19	0.40	0.01
			30	12.5	20.8	23.1	0.15	0.27	0.02
			60	12.5	17.3	10.7	0.06	0.13	0.02

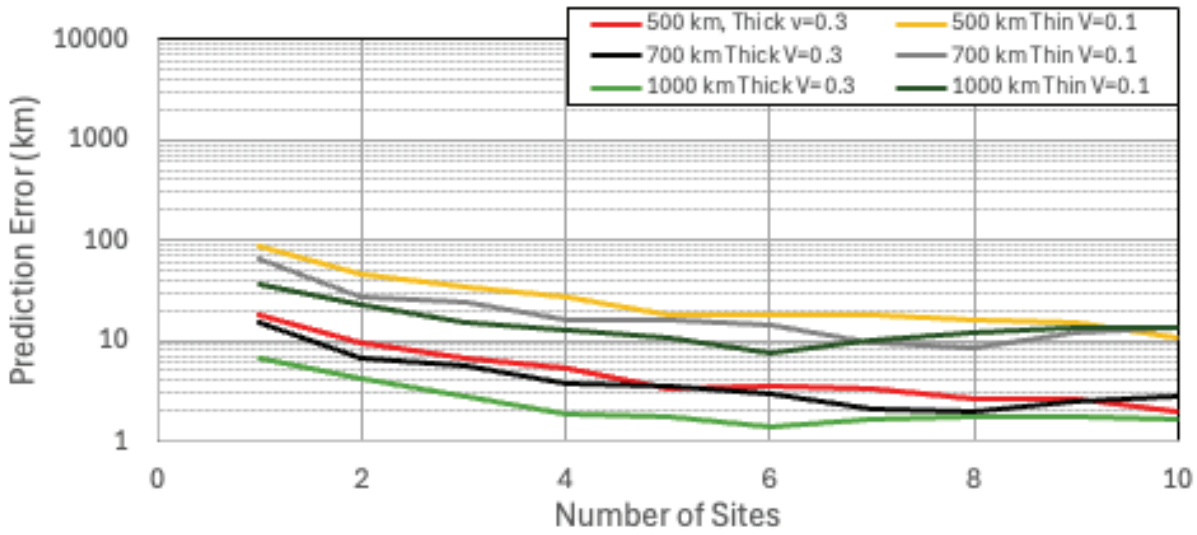

Figure 4.3-1. Average SPOE prediction accuracy (1σ) at the next track, as a function of the number of sites

The errors in Figure 4.3-1 lead to a worst case (3σ) duration of +/- 0.12 minutes for the "thick" FoV case to hold open a cued search at the next track for a newly discovered uncorrelated track (UCT). Even for the "thin" case the duration is only +/- 0.58 minutes Both cases however are acceptable in terms of power aperture for a low-cost radar; however, a "thicker" case FoV, with a minimum track arc of ~17.5° is preferable.

4.3.3 Multi-track orbit accuracy

Three-day orbit solutions were generated for the "thin" and "thick" FoV cases. Figure 4.3-2 shows the error prediction including drag (1σ) at a nominal 24-hour prediction. These results were computed for low solar flux conditions. Drag was estimated over the three-day solution period and the estimated drag parameter included in the predictions. Three days of tracking data were included, followed by 1 day of prediction. Performance values were computed at 4 days from the start of the run; for the 1 and 2 site cases, the predictive periods were up to 2 days past the last sensor track due to limited sensor visibility, resulting in longer predictions and higher errors.

Prediction accuracy was typically 10 m or better (1σ). There is little practical difference in the multiday orbit solutions between the two FoV configurations. Both the thin and thick cases produce similar results at a practical level. Above 500 km there is a general improvement with the number of sites. As a general practice, the estimation strategy for optimal orbit accuracy should be tuned to account for the drag conditions, including ballistic coefficient, as well as the frequency of tracking. Typically, a higher rate of tracking will support a more frequent drag estimation, resulting in better orbit solution accuracy, and potentially better orbit prediction accuracy.

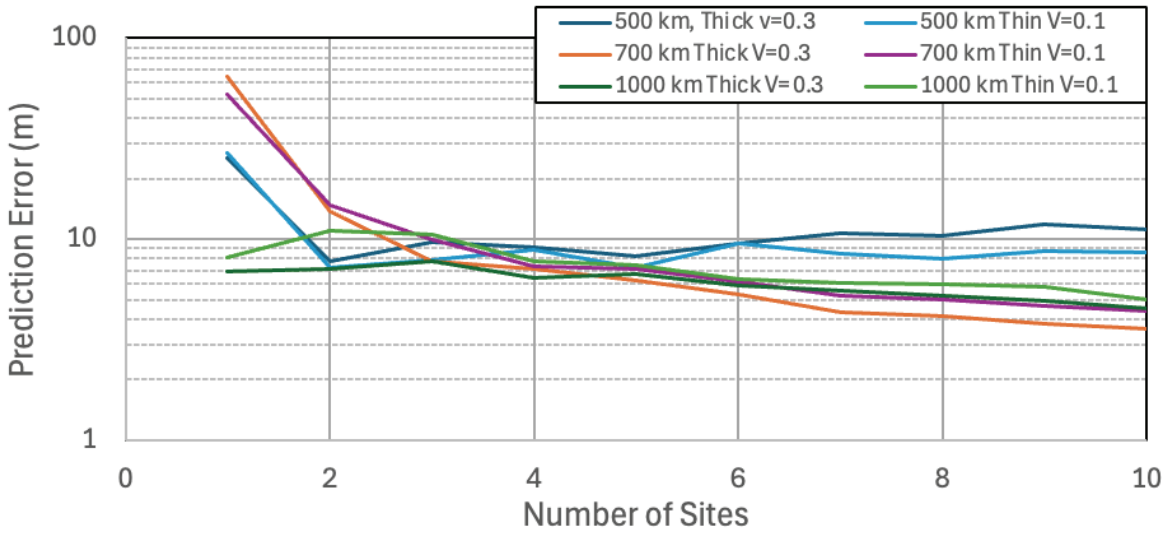

Figure 4.3-2. Three-day orbit solution prediction errors (1σ), including drag, after a nominal 1 day prediction, as a function of the number of sites

4.4 RSO Maneuver Considerations

The ability to accurately detect and recover the orbit for an RSO that has maneuvered is critical for maintaining custody of the object. Ideally a sensor system will be able to automatically detect the maneuver, identify the time and location, and then estimate post maneuver predictions with no operator-in-the-loop processing. Key to this is having the timeliness to detect the maneuvers quickly, before the orbit errors caused by the maneuver get so large that the known RSO is lost due to inability to cue a track at the next sensor, or a lack of processing to associate a new UCT back to the known orbit estimates.

To demonstrate this capability with a network of smaller dispersed sensors, a range of orbit maneuver sizes were considered in this analysis. First, it is necessary to place the maneuver magnitudes in perspective. For this example, the ICESAT mission reference orbit station keeping was used [5]. At 600 km altitude, drag makeup maneuvers near solar maximum are typically <0.1 m/s dV in-track every 10 days to maintain a ground track that is within 800 m of the nominal reference mission orbit. Inclination control to maintain the same ground track requires about 1.5 m/s of cross track dV every 4 months.

Maneuvers in the 1 m/s to 10 m/s dV in track are used to change orbit phasing, raise or lower the orbit to drift the local solar time, or for rendezvous with another spacecraft. Shown in Figure 4.4-1 are the expected prediction accuracies for in track maneuvers of 1 and 10 m/s over a single day. These are shown on the same scale as the SPOE prediction errors (Figure 4.3-1) for comparison. The prediction errors caused by not modeling the maneuver are large, and for a single sensor, which may only be able to see an object every 12 or 24 hours (18 hours on average in the cases shown in Section 4.2), represent a large uncertainty window for the sensor FoV penetration. Expressed in terms of time, a search window will need to be held open for +/- 12.4 minutes (3σ) at 500 km, decreasing to 6.3 minutes at 1000 km to catch an object capable of performing a 10 m/s dV. While a single search window will not consume much power aperture resource, using this approach for many spacecraft at a time drives towards the need for an uncued search fence which drives up cost, especially at 1000 km. By comparison the time required to hold open a search with 10 sites is <1.1 minutes (3σ) for larger burns, with is much more tractable.

Moreover, if multiple sensors are used, the prediction error at the next expected sensor penetration decreases significantly. This can typically be accommodated from a small, cued search to initiate a track. This has two major benefits: 1) it makes breaking custody of a maneuvering RSO much harder to achieve, and 2) it greatly reduces the power-aperture required at each sensor. The savings in cost resulting from the elimination of wide uncued search fence enables more sensors, an improved timeliness of event detection, and better custody management.

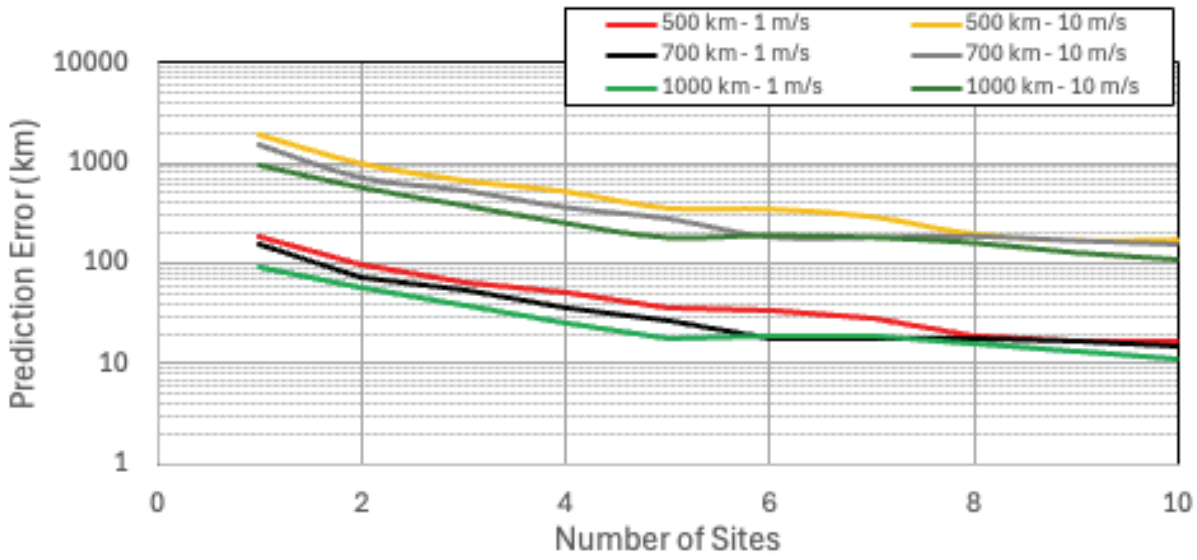

Figure 4.4-1. Prediction errors at next track for 1 and 10 m/s dV vs number of radar sites

4.5 Maneuver Magnitude Estimation

Maneuver estimation accuracy was estimated in a limited set of runs for a few techniques. Example results are shown in Table 4.5-1:

1. Estimation of the maneuver magnitude using a single track after the maneuver, compared to the non-maneuver case: This technique is limited by the SPOE accuracy, and is of limited utility for most cases.

2. Using pre-maneuver data to constrain the estimation of the maneuver dV in a constrained Bayesian orbit solution for the post maneuver state: When a track is detected on a known object that is a significantly off from the nominal prediction and does not fit with the track data, the SPOE can be back propagated to determine when it conjuncts with the pre-maneuver orbit. The radial and cross track error estimates, and the RSO location from the pre-maneuver multi-day solution at the predicted time of conjunction, can be used to constrain a post-maneuver orbit solution using the single track. Uncertainty in the knowledge of the time of the maneuver is estimated by using the uncertainty of the post-maneuver track expressed at the conjunction time to constrain the along-track position. Using these constraints, a post-maneuver orbit solution is executed using the post-maneuver track. The estimated velocity uncertainties at the start of the solution (corresponding to the assessed maneuver time) represent the maneuver dV uncertainty.

Table 4.5 -1. Estimated dV accuracies

Approach	Accuracy (m/s)			Comments
Assessment from SPOE difference with prediction	Thin FOV: ~20 Thick FOV: ~5			See Table 4.3-1; results are strongly dependent on FOV penetration geometry
Constrained with pre-maneuver orbit	Thin	500 km alt	0.46	Cases were run for worst case fly through performance at the center of the FOV with azimuth = 0°. See Table 4.3-1.
		700 km alt	0.79	
		1000 km alt	1.06	

	Thick	500 km alt	0.25	
		700 km alt	0.28	
		1000 km alt	0.30	

As shown in Table 4.5-1, use of pre-maneuver data from this class of sensor can provide greatly enhanced maneuver accuracy estimation, as compared to a single track. More study is required on this subject; however, these results indicate that with appropriate processing support this class of sensor can provide timely assessment of spacecraft maneuvers with very high accuracy.

3. SUMMARY AND CONCLUSIONS

This paper has outlined how a cost-effective global network of small LEO surveillance radars can be made feasible by leveraging a LFoV architecture for the radars, and by sharing the required global power – aperture among the network radars. This system approach distributes the functions of orbital determination and discovery of space events over a global network of small radars, yielding accurate state vector updates on a roughly 1 hour time scale. This paper has also shown that accurate state vectors can be obtained even for orbits traversing a narrow FoV having widths of the order of 0.2 in v. This paper outlined how reducing $<P>A_r$ at each radar can lower its cost and that of the network. The result of this architectural strategy is a global network of radars that provides approximately hourly updates of space object state vectors, high accuracy propagation of orbits, and discovery of space events on a 5-10 hour time scale.

Of course, this analysis and the general examples shown are intended to strategically guide network architectural design. Design details, however, need to be determined based on detailed requirements and simulations of the scenarios of interest. Nevertheless, it is hoped that this paper spurs thought and ultimately results in the fielding of a global cost-effective LEO multi-radar network.

4. REFERENCES

[1] Mathematical Description of the ORAN Error Analysis Program, W. Hatch, C. Goad, Wolf Research and Development Corporation, 1973.

[2] The Operations Manual for the ORAN Multi-Satellite Error Analysis Software, J. J. McCarthy, DLR German Space Operations Center, 2024.

[3] A. C. Long, J. O. Cappelari, Jr., C. E. Velez, A. J. Fuchs, Goddard Trajectory Determination System (GTDS) Mathematical Theory Revisions 1, Computer Sciences Corporation, July 1999.

[4] GEODYN Systems Description Volume 1, J. W. Beall, J. J. McCarthy, S. Rowton, D. Moore, D. E. Pavlis, S. B. Luthcke, L. S. Tsaoussi, NASA GSFC, 2015.

[5] Overview of the ICESat Mission , B. E. Schutz, H. J. Zwally, C. A. Shuman, D. Hancock, and J. P. DiMarzio GEOPHYSICAL RESEARCH LETTERS, VOL. 32, L21S01, doi:10.1029/2005GL024009, 2005.